RESEARCH ARTICLE | MAY 16 2023

Bright single-photon emission from a GeV center in diamond under a microfabricated solid immersion lens at room temperature

J. Christinck ✉; F. Hirt; H. Hofer; ... et. al

Check for updates

CrossMark

View Online

Export Citation

Articles You May Be Interested In

Back Matter for Volume 1208

AIP Conference Proceedings (January 2010)

CPV module based on a hybrid solar cell

AIP Conference Proceedings (August 2019)

The Feasibility of a Stretched Lens Concentrating Solar Array Direct-Driving an Electric Thruster

AIP Conference Proceedings (January 2010)

Bright single-photon emission from a GeV center in diamond under a microfabricated solid immersion lens at room temperature

J. Christinck,[1,a),b)] F. Hirt,[1,b)] H. Hofer,[1] Z. Liu,[2,b)] M. Etzkorn,[2,b)] T. Dunatov,[3] M. Jakšić,[3] J. Forneris,[4,c)] and S. Kück[1,b),d)]

AFFILIATIONS

[1] Physikalisch-Technische Bundesanstalt, Bundesallee 100, 38116 Braunschweig, Germany
[2] Technische Universität Braunschweig, Universitätsplatz 2, 38106 Braunschweig, Germany
[3] Ruđer Bošković Institute, Bijenička cesta 54, 10000 Zagreb, Croatia
[4] Physics Department, University of Torino, Via P. Giuria 1, 10125 Torino, Italy

a) Author to whom correspondence should be addressed: justus.christinck@ptb.de
b) Also at: Laboratory for Emerging Nanometrology, Langer Kamp 6a/b, 38106 Braunschweig, Germany.
c) Also at: Instituto Nazionale di Ricerca Metrologica (INRiM), Strada delle Cacce, 91, 10135 Torino, Italy and Istituto Nazionale di Fisica Nucleare (INFN), Via P. Giuria 1, 10125 Torino, Italy
d) Electronic mail: stefan.kueck@ptb.de

ABSTRACT

We report on the metrological characterization of the emission from a germanium-vacancy center in diamond under a microfabricated solid immersion lens in a confocal laser-scanning microscope setup. Ge ions were implanted into a synthetic diamond at 3 MeV, and germanium-vacancy centers were then formed by subsequent annealing. Afterward, solid immersion lenses were fabricated in a focused ion beam scanning electron microscope. The photoluminescence was investigated at room temperature in terms of the spectral distribution, the excited state lifetime, the second-order correlation function, and the saturation behavior, proving simultaneous high single-photon purity and high brightness. Two methods were exploited to minimize the residual multi-photon probability: spectral filtering and temporal filtering. According to these results, we assume that Raman scattered photons and emission from neighboring color centers play an important role in the residual multi-photon emission probability. The system efficiency of the single-photon source was investigated and found to be in accordance with the value calculated from all sources of loss in the setup. The branching ratio of the germanium-vacancy center for the decay into the ground state and into metastable state was calculated. The results enable the usage of the single-photon source in future quantum radiometric experiments.

I. INTRODUCTION

Single-photon sources are of interest in many applications, such as quantum key distribution, quantum information processing,[1,2] as well as in quantum metrology.[3,4] The nitrogen-vacancy (NV) center in diamond is well-studied[4–12] and easily accessible due to the natural presence of nitrogen and NV centers in type Ib diamond.[13] Recently, color centers based on germanium-vacancy (GeV),[14–18] tin-vacancy (SnV),[19–23] lead-vacancy (PbV),[24,25] and magnesium-vacancy

(MgV)[26] grew in interest because of their narrow luminescence spectrum and their bright emission. The broad spectral distribution was the most significant contributor to the standard uncertainty in the determination of the spectral photon flux for an NV center in recent quantum metrological experiments.[27] Therefore, the reduction of the spectral width of the single-photon emission from diamond color centers is of utmost importance. The GeV center has a strong zero-phonon line emission at 602 nm[14,15,28] with a Full Width at Half

Maximum (FWHM) at room temperature of 5 nm[28] and its phonon sideband emission is weak, indicated by a Debye–Waller factor of 0.6[29] compared to that of the NV center of 0.03.[30] The excited state lifetime is 5 ns to 6 ns,[18,28,31] and thus significantly lower than for NV centers.[11] These parameters render it a promising candidate for future quantum metrological experiments at room temperature. Hence, it has been chosen for experimental investigation in this work.

The extraction of photons from diamond, which have been emitted by such a color center, is severely limited due to the high refractive index of diamond (n = 2.415 at 600 nm[32]) and the corresponding angle of total internal reflection of 24.5°. Only $\approx 8.5\%$ of the emitted photons from a color center in diamond can leave the crystal[33] and only $\approx 5.1\%$ are collected when using a microscope objective with an NA of 0.9.[34] This contrasts with nanodiamond samples, where the total internal reflection is suppressed and the angular emission follows the pattern of a free dipole in air,[35] neglecting the negative effect of the high refractive index of the diamond. Moreover, the interface to a cover glass can enhance the emission properties due to the coupling of evanescent waves into the glass, leading to collection efficiencies of more than 80% for NV centers in nanodiamond.[11] In bulk diamond, there are several approaches to enhance the collection efficiency of a single-photon emitter, which can be sorted into two categories. First, resonant approaches, whereby changing the local electromagnetic boundary conditions one can alter the photonic mode density,[33] thus enhance the photon emission via the Purcell effect[36] and spatially confine the emission. Second, geometric approaches, where, e.g., the geometric shape of the crystal surface is changed so that more photons will be extracted from the diamond. Whereas the former can also confine the spectral distribution of the emitted photons,[21] the latter is more straightforward and easily accessible, e.g., by fabricating a semi-hemispherically shaped diamond crystal[37] or by placing gallium phosphide (GaP) lenses[38–40] or zirconium dioxide (ZrO₂) lenses[41] onto the sample. Such solid immersion lenses (SILs) can also be fabricated on a microscopic scale using the focused ion beam (FIB) technique,[42–44] which has been shown to enhance the count rate from an NV center by a factor of 3.4,[44] 8,[43] and up to 10.[42] Using this method, individual emitters are targeted and SILs are fabricated around the emitter. This approach was chosen for the diamond sample investigated in this work.

II. SOLID IMMERSION LENSES

A. Principle

Photons emitted from a color center in planar diamond are bound to the diamond medium with a high percentage due to total internal reflection and even if they can leave the diamond, they are refracted to higher angles. This is illustrated in Fig. 1. Thus, collecting photons from diamond crystals is inefficient. The most straightforward way to enhance the photon outcoupling from a diamond is to change the shape of the surface so that no photon reaches it with an angle higher than the angle of total internal reflection. Then, only the Fresnel reflection and non-unity numerical aperture of the collection optic hinders the photon's transmission into the detection path. If the diamond surface is shaped into a semi-hemisphere with the emitter in the center, as shown in Fig. 1, the direction of propagation of all photons is perpendicular to the surface and, therefore, no refraction
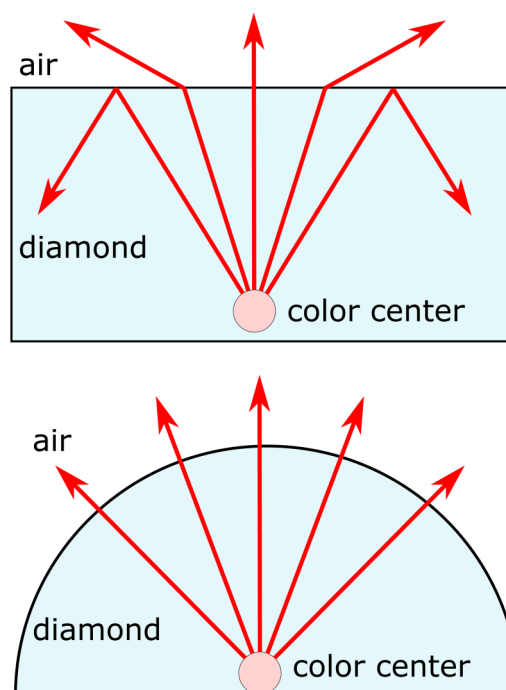

FIG. 1. The principle of the semi-hemispherical SIL in diamond: photons are coupled out more efficiently than from a planar surface because total internal reflection does not occur and refraction into higher angles is avoided.

to higher angles occurs. Such a plano–convex lens is called semi-hemispherical solid immersion lens.[9,37–42,44] There is a second configuration of solid immersion lenses, called Weierstrass configuration.[33] Although it may have slightly superior properties regarding the numerical aperture of its emission, the semi-hemispherical solid immersion lens is much simpler to fabricate into the diamond surface using the focused ion beam technique. The semi-hemispherical SIL is, therefore, the most straightforward way to enhance the collection efficiency from a color center in diamond.

B. Enhancement of the collection efficiency

The collection efficiency η in the meaning of the proportion of photons collected by the microscope objective divided by all emitted photons for a dipole oriented parallel to the surface is estimated by[33]

$$\eta = \frac{15}{32}\left(1 - \sqrt{1 - \left(\frac{NA}{n_1}\right)^2}\right) + \frac{1}{32}\left(1 - \cos\left[3\arcsin\left(\frac{NA}{n_1}\right)\right]\right),$$

(1)

where NA is the numerical aperture of the objective and n_1 is the refractive index of the diamond. Using this equation, the above-mentioned estimation of 5.1% collection efficiency from color centers in planar diamond was made. In this equation, the Fresnel reflection at the diamond-to-air interface is not considered. As a

rough estimation, the Fresnel factor for perpendicular incidence could be used, which is

$$T = 1 - \left[\frac{n_1 - n_2}{n_1 + n_2}\right]^2, \qquad (2)$$

where n_2 is the refractive index of the medium between the diamond and the microscope objective. One could consider this to be an upper boundary for the transmission coefficient because the light reaching the interface at higher angles will be reflected with a higher percentage or reflected completely when reaching the angle of total internal reflection. This simplification must be made since the Fresnel transmission coefficient generally depends on the polarization of the light in the general case. For diamond, this gives $T \approx 82.8\%$. For a rough estimation of the collection efficiency, the product of Eqs. (1) and (2) was calculated. The total collection efficiency of the emission from a color center located below a planar diamond surface is then 4.3% in the case of an NA of 0.9. It increases for a semi-hemispherical SIL to 27.0%, again with an NA of 0.9 by using $n_1 = 1$ in Eq. (1).[34] This means at least a sixfold increase in the collection efficiency, when the SIL is perfectly fabricated, i.e., the shape is semi-hemispherical and the emitter is located in the center of the SIL.

III. EXPERIMENTAL METHODS

A. Sample fabrication

A $2 \times 2 \times 0.5\,mm^3$ detector grade diamond from Element Six was used for the production of a GeV center sample. This diamond contains very few impurity atoms in its lattice, which is optimal for the production of isolated color centers by implantation. Ge^{2+} ions have been implanted into the diamond at 3 MeV energy using a broad beam scanned to obtain a homogeneous size of $1.5 \times 1.5\,cm^2$. The sample was exposed to the beam for 10 s with a current of 7.5 nA of Ge^{2+} ions, leading to a total fluence of roughly $10^{11}\,cm^{-2}$. To ensure the generation of isolated color centers, a mask of aluminum foil was placed roughly $50\,\mu m$ over the diamond. This allowed the scattering of a portion of the germanium ions at the edge of the aluminum foil and the subsequent implantation of single ions around the implanted region. This implanted region itself had an ion density too large to contain single color centers. Nevertheless, it enabled easy alignment of the setup due to the strong photoluminescence from multiple color centers in the confocal volume and, therefore, high count rates even with suboptimal optical alignment of the setup. The high-density implanted area was, therefore, useful for alignment purposes. A simulation of the implantation depth according to the software "Stopping Ranges of Ion Matter"[45] gives an estimated mean depth of the germanium ions of $(1.12 \pm 0.13)\,\mu m$. Due to the scattering, the isolated color centers outside the implanted region may be of shallower depth.

The formation of color centers from the implanted germanium ions and vacancies in the diamond lattice was performed in a high-temperature annealing process at 1200°C for 2 h in vacuum (pressure $< 5 \times 10^{-6}$ mbar). At this temperature, vacancies in the diamond lattice become mobile and are then trapped by germanium ions, which leads to the formation of stable germanium-vacancy (GeV) color centers. The germanium ion takes an interstitial position between two vacant positions in the lattice [see Fig. 2(a)].[14,28,31] The high-temperature annealing also heals the diamond from damages caused by the implantation process, such as local strain and stress.

To remove residual non-diamond carbon, which was formed during the annealing process,[21] and other contamination from the surface, the diamond was cleaned in an O_2 plasma and then treated in an acid bath for 4 h at 80°C using a 3:1 mixture of 96% sulfuric acid and 70% nitric acid. In this procedure, the diamond surface was chemically homogenized, enabling a higher single-photon purity from the color center emission.[46] Finally, the sample
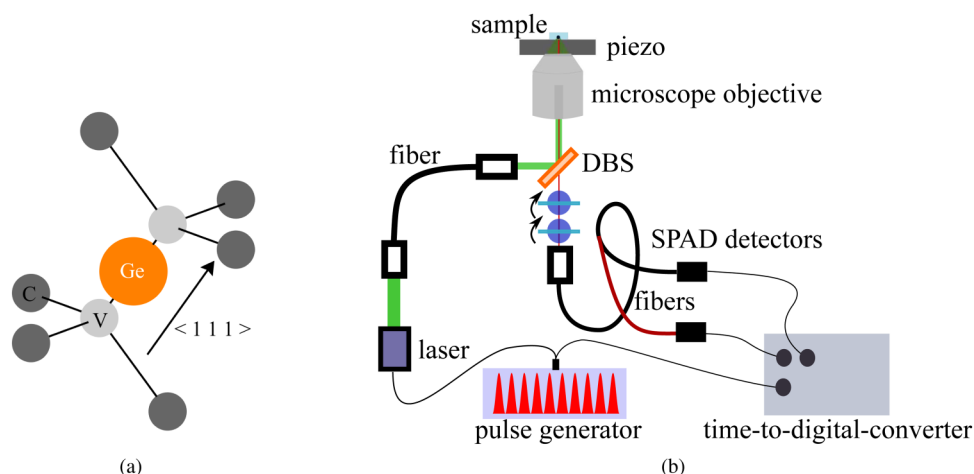
FIG. 2. (a) The diamond lattice with a Ge ion in an interstitial position between two vacant positions, forming a GeV center, (b) experimental setup for characterization of the emission of GeV centers. DBS: dichroic beam splitter, SPAD: single-photon avalanche diode.

was brought into an oven at 450°C in air at ambient pressure for 24 h to clean the sample surface from the last contamination and to enable proper surface termination.

B. SIL milling process

Semi-hemispherical solid immersion lenses were milled into the diamond surface using a dual-beam focused ion beam scanning electron microscope (FIB-SEM) setup (Helios 5 UX Dual Beam, Thermo Fisher). The focused ion beam consisted of 30 kV gallium ions, and a current of 0.75 nA was chosen for the milling process. To create the SIL, we defined a local ion beam exposure map with a lateral resolution of 456×456 pixels^2 over a $2 \times 2 \mu m^2$ image with 256 different exposure levels. An example of a SIL produced with the FIB in this way is shown in Fig. 3. Since diamond is a good electrical insulator, there were issues with local charging that deflected the ion beam. The effect can also be seen in the upper-right corner of Fig. 3. This effect makes it difficult to place a lens directly onto a pre-characterized GeV center since the field of view (FOV) of a SIL is small. It can be calculated with[44]

$$d_{\text{FOV}} < \sqrt{\frac{d\lambda}{n(n-1)}}, \qquad (3)$$

where n is the index of refraction, λ is the emission wavelength, and d is the diameter of the SIL. For a SIL with a diameter of $1 \mu m$ this results in $d_{\text{FOV}} \approx 420$ nm. Since smaller SILs enhance the chance to find just one GeV center inside, a trade-off between two very practical problems arises. Larger SILs make it easier to selectively place the SIL on top of a GeV center in a known location relative to markers on the diamond surface, whereas smaller SILs have a higher chance of single-photon emission due to their smaller field of view. Therefore, on our sample, arrays of SILs were milled semi-randomly into suitable areas on the diamond surface. For SILs with a radius smaller than the implantation depth of the color centers, as much diamond was
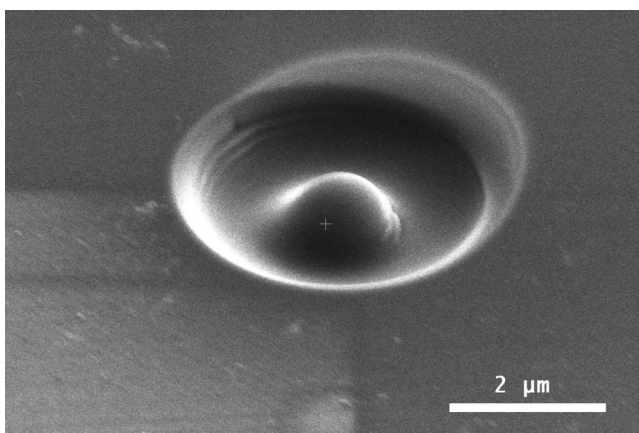

FIG. 3. Example of a SIL fabricated by FIB and imaged by SEM at 5 kV and 0.1 nA with a tilt of 52° from the surface normal.

removed beforehand so that the new depth of the color centers would again match the desired SIL radius. The highest success was reached when fabricating small SILs with a diameter of $1 \mu m$ into areas of low emitter density. For that reason, most SILs were dark, meaning either no color center was below or the color center was not aligned with the center. Still, some SILs contained a GeV center with very bright emission.

C. Experimental setup

1. Confocal microscope

The photoluminescence of the GeV centers was characterized in a self-built confocal microscope setup, which is schematically shown in Fig. 2(b). For the excitation of the emitters, an externally triggered (33611A, Keysight) laser (Prima, Picoquant) with continuous wave and pulsed emission at 515 nm up to a repetition rate of 200 MHz was used. After outcoupling into the free-space setup using a 10× objective (RMS10X, Thorlabs), a continuous neutral-density wheel (NDC-100S-4M, Thorlabs) was used to quickly tune the power of the incident laser beam for the experiment. The beam was directed to a microscope objective (100×, NA 0.9, Plan Apo HR 100X, Mitutoyo) by a dichroic beam splitter (DMLP550, Thorlabs). The photoluminescence was collected by the same objective, transmitted by the dichroic beam splitter and filtered by two tunable edge filters (TLP01-628 and TSP01-628, Semrock) mounted on precision rotation mounts (RS-40, Physik Instrumente). A 10× objective (RMS10X, Thorlabs) focused the light onto a single-mode optical fiber (P1-630A, Thorlabs), which was used as the pinhole of the confocal setup. The photoluminescence was then characterized using a spectrometer (Acton SpectraPro SP-2500 monochromator with Pylon PYL-100BRX-NS-SM-Q-F-S camera, Princeton Instruments) and a Hanbury Brown and Twiss interferometer consisting of two SPAD detectors (SPCM-AQRH-14-FC, Excelitas) and a fiber-based 50:50 beam splitter (TW630R5F1, Thorlabs). The alignment of the sample was performed using a wide-field microscope configuration using a small LED and a minicam (DCU224/M-GL, Thorlabs). The sample is moved by a piezo translation stage (P-563.3CD stage, Physik Instrumente). A time-to-digital-converter (Time Tagger Ultra, Swabian Instruments) served as the correlator in the Hanbury Brown and Twiss configuration and for the detection of the photon count rate.

2. Timing resolution of the detection system

When measuring the second-order correlation function $g^{(2)}(\tau)$ using a continuous wave laser, the single-photon purity is determined by the value $g^{(2)}(\tau = 0)$. The measurement data taken from a Hanbury Brown and Twiss setup are usually fitted using a three-level scheme to consider the effect of a third metastable (shelving) state[4,13]

$$g^{(2)}(\tau) = 1 + c_2 \exp\left[-\frac{|\tau|}{\tau_2}\right] + c_3 \exp\left[-\frac{|\tau|}{\tau_3}\right], \qquad (4)$$

where c_2 and c_3 describe the strength of the anti-bunching and bunching processes on short and intermediate times intervals, respectively.[47] In addition, τ_2 and τ_3 are the state lifetimes in the

experiment, which depend on the excitation power.[48] Due to the timing resolution of the detection system, the two avalanche diodes and the Time Tagger, the measured histogram is a convolution of Eq. (4) with the instrument response function, which can be represented in good approximation using a Gaussian function. This convolution was calculated as[49]

$$
\begin{aligned}
g^{(2)}(\tau) = 1 &+ \frac{c_2}{2} \, \exp\left(\frac{-\tau}{\tau_2} - \frac{\sigma^2}{2\tau_2^2}\right) \operatorname{erfc}\left(\frac{\sigma^2 - \tau\tau_2}{\sqrt{2}\sigma\tau_2}\right) \\
&+ \frac{c_2}{2} \, \exp\left(\frac{\tau}{\tau_2} - \frac{\sigma^2}{2\tau_2^2}\right) \operatorname{erfc}\left(\frac{\sigma^2 + \tau\tau_2}{\sqrt{2}\sigma\tau_2}\right) \\
&+ \frac{c_3}{2} \, \exp\left(\frac{-\tau}{\tau_3} - \frac{\sigma^2}{2\tau_3^2}\right) \operatorname{erfc}\left(\frac{\sigma^2 - \tau\tau_3}{\sqrt{2}\sigma\tau_3}\right) \\
&+ \frac{c_3}{2} \, \exp\left(\frac{\tau}{\tau_3} - \frac{\sigma^2}{2\tau_3^2}\right) \operatorname{erfc}\left(\frac{\sigma^2 + \tau\tau_3}{\sqrt{2}\sigma\tau_3}\right),
\end{aligned}
\tag{5}
$$

where σ is the timing jitter of the detection system (standard deviation) and erfc is the complementary error function. The convolution results in a rounding of the tip of the anti-bunching dip at $\tau = 0$. This effect can be seen in Fig. 4(a), where the experimental data follow Eq. (5). To compensate for the effect of the timing jitter, Eq. (5) was used to fit the experimental data and the timing jitter-independent single-photon purity was calculated from $g^{(2)}(0) = 1 + c_2 + c_3$. No other correction, e.g., dark count correction or background correction, was carried out.

A measurement of the timing jitter of the detection system and its Gaussian fit are shown in Fig. 4(b). The standard deviation σ of the fit is (293 ± 2) ps, which corresponds to a timing jitter (FWHM) of (690 ± 5) ps, where the uncertainties of these values were calculated by taking the 95% confidence interval of Student's t

distribution. This timing jitter was used for the evaluation of the auto-correlation function $g^{(2)}(\tau)$.

3. Spectral filtering of the fluorescence

The fluorescence from the sample was spectrally filtered using a long-pass and a short-pass tunable edge filter similar to earlier reports, where two bandpass filters were used to filter the spectral line corresponding to a specific excitonic recombination process of a quantum dot.[50] These tunable filters alter their edge wavelength with the angle of the incident beam. Both filters have a zero angle edge at roughly 635 nm and at the maximum rotation of 60° the edge wavelength is at roughly 555 nm. In the experiment, the filters were placed on a rotation mount so that the angle of incidence is changed by rotation of the filter, which is illustrated in Fig. 5. By rotation of the long-pass filter to an angle of 40°, the GeV center emission between approximately 590 and 635 nm was transmitted. The spectral distribution of the emission was changed on demand to be able to, e.g., measure only the zero-phonon line emission using angles of 31° and 38° for the short-pass and long-pass filter, respectively. Then, the transmission window of the two filters ranged from 598 to 610 nm.

IV. RESULTS

A. Transmission of the setup

The transmission of photons from the diamond to the detectors was estimated by measuring the intensity reduction of a laser with a wavelength of 640 nm for each optical element in the fluorescence path from the sample to the microscope objective in front of the optical fiber. In detail, this is the microscope objective, a mirror, the dichroic beam splitter, the two tunable edge filters, and the microscope objective that was used for fiber coupling. The
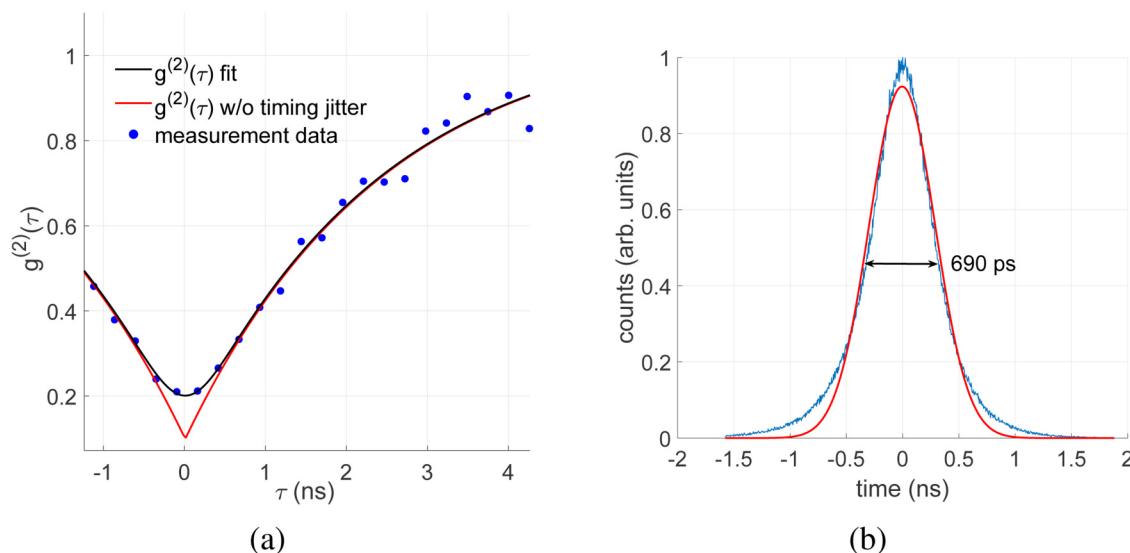
(a)   (b)

FIG. 4. (a) The measured $g^{(2)}(\tau)$ function of a GeV center with the fit according to Eq. (5) (red). The "real" $g^{(2)}(\tau)$ function, independent of the timing jitter of the detection system, is shown in black, (b) measurement data (blue) of the timing resolution of the confocal microscope setup's detection system and a Gaussian fit (red).
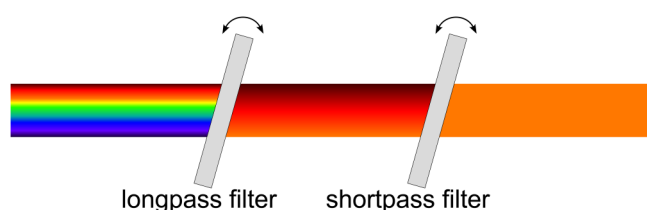
FIG. 5. A sketch of the spectral filtering using a long-pass edge filter and a short-pass edge filter on two rotation mounts.

combined transmission to the pinhole was determined to be $(60 \pm 4)\%$. This is a significant reduction of the losses compared to earlier reports,[51] where the transmission of a similar setup was calculated to be 34%. The enhancement of the transmission was made possible by the utilization of the tunable edge filters with a very high transmission coefficient and high suppression of the blocked wavelengths, yielding roughly $(94 \pm 5)\%$ transmission from the spectral filtering. The microscope objectives in front of the sample and the fiber, as well as the dichroic beam splitter were chosen because of their high transmission of $(76 \pm 2)\%$, $(91 \pm 2)\%$, and $(92 \pm 1)\%$, respectively. The coupling efficiency of the emitted mode from the single-photon emitters into the single-mode fiber could only be estimated to be (60 ± 20). The losses in the optical fiber were neglected due to the insignificant length of the optical fiber of only 1 m. The combined transmission from the first microscope objective to the detector, which includes the fiber coupling efficiency, was determined to be $(36 \pm 12)\%$.

B. Proof of successful fabrication of single GeV centers

Prior to the fabrication of SILs, the sample was investigated in the confocal microscope setup to verify the successful generation of GeV centers. Isolated single-photon emitters were found in the vicinity of the ion implantation region due to the scattering of some ions at the edge of the aluminum foil mask. A

photoluminescence scan with one bright emitter marked is shown in Fig. 6(a). The emitter's emission was investigated in terms of the spectral distribution [see Fig. 6(b)] and the single-photon purity by measuring $g^{(2)}(\tau)$ [see Fig. 6(c)]. The zero-phonon line (ZPL) of this emitter is at 604.2 nm with a FWHM of that peak of 7.5 nm. The literature value of the ZPL wavelength is 602 nm[14,15,28] but, nevertheless, the emission was attributed to a GeV center. A possible explanation for the shift of the ZPL could be local strain and stress in the diamond lattice, created by the implantation of the Ge ions, which did not cure completely in the annealing process. The Hanbury Brown and Twiss measurement data were fitted using Eq. (5), revealing $g^{(2)}(\tau = 0) = 0.20 \pm 0.07$ and therefore proving single-photon emission from this GeV center. Similarly, some other isolated, bright spots were investigated and GeV center emission's spectral distribution and $g^{(2)}(\tau = 0) < 0.5$ were found for most of them. The count rate in the experiment did not exceed 150 kcps, leaving space for the enhancement of the count rate through the fabrication of a solid immersion lens.

C. Single-photon emission from a GeV center in a SIL

Solid immersion lenses were fabricated with a diameter of $1\,\mu m$ according to the procedure introduced in Sec. III B. In Fig. 7, the metrological characterization of the emission of one GeV center in a SIL is shown. The emitter, marked by the red circle, is located in the vicinity of the implanted area, which is the bright area on the left side of Fig. 7(a). The spectral distribution of the emission revealed a ZPL at 602.9 nm and an FWHM of 6.3 nm [see Fig. 7(b)]. The cut-off at 635 nm was chosen for maximal transmission, which would be worse at higher wavelengths, since a different tunable short-pass filter would be needed. A second curve is shown, which was measured by changing the angles of the tunable edge filters in the setup, where the edge wavelength of the long-pass filter and the short-pass filters were set to 598 nm and 610 nm, respectively. The FWHM of that curve has shrunken slightly to 6.1 nm due to the narrow filtering. The excited state lifetime was measured by taking the laser pulses at a repetition rate of $f_{rep} = 2\,MHz$ as a

(a)

(b)
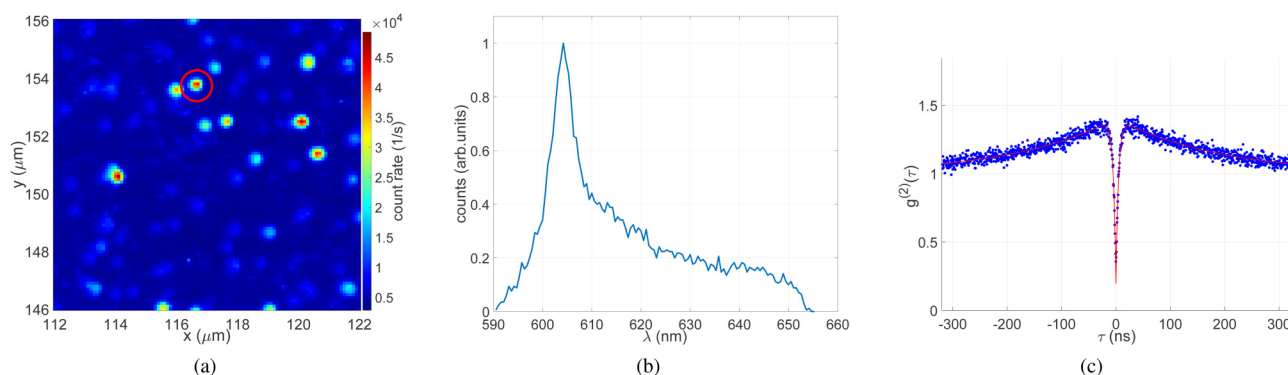
(c)

FIG. 6. (a) The photoluminescence map of the investigated area on the diamond surface near the implanted area, where each spot likely corresponds to a GeV center, (b) the spectral distribution of the emission of the color center marked with the red circle, which clearly shows GeV center emission, (c) the second-order correlation function $g^{(2)}(\tau)$ measured from the same emitter.
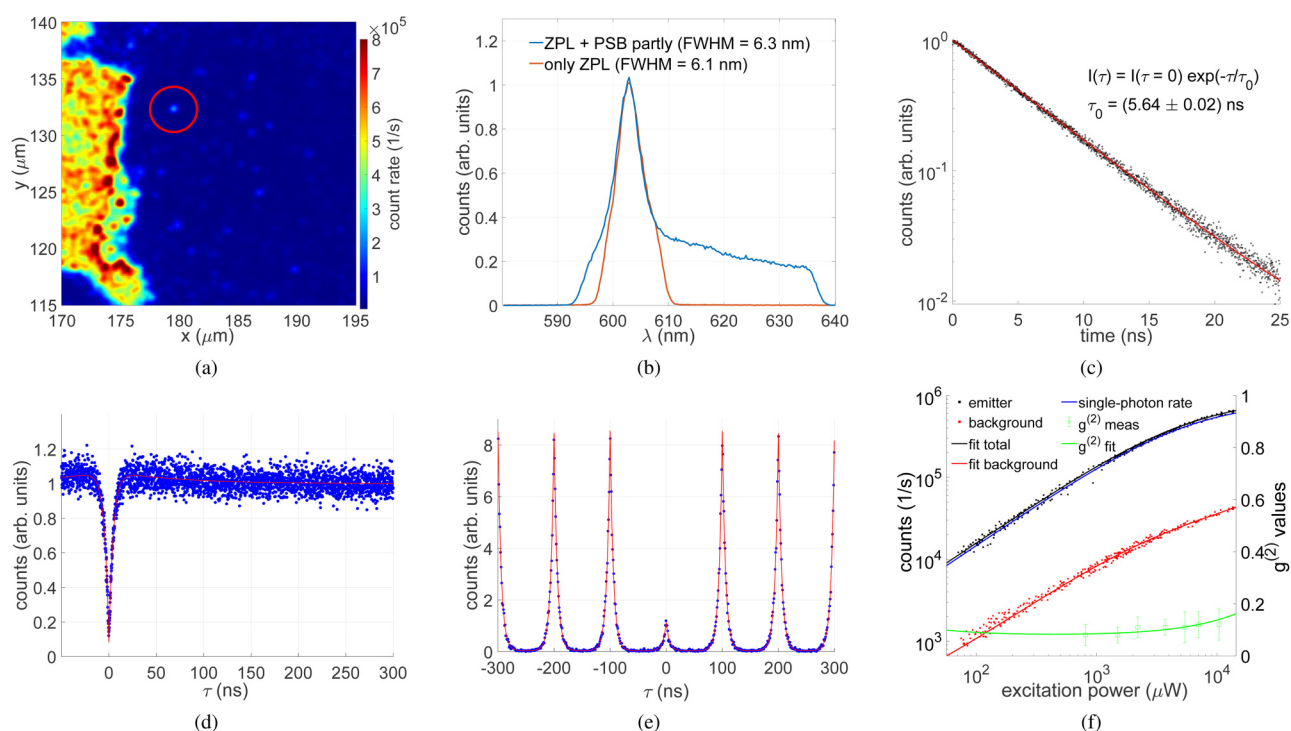
FIG. 7. (a) The photoluminescence map of the area where a bright and high single-photon purity emitting GeV center was found in a solid immersion lens (red circle), (b) the spectral distributions of the GeV center emission for different angles of the tunable edge filters, (c) the excited state lifetime measured by correlation of laser pulses and the arrival of a photon from the GeV center, (d) the second-order correlation function $g^{(2)}(\tau)$ measured with continuous wave excitation and (e) with pulsed excitation at a repetition rate of $f_{\text{rep}} = 10$ MHz, (f) the saturation curve of the GeV center emission.

reference signal and calculating the exponential decay of the excited state. The data were fitted using the equation $I(\tau) = I(\tau = 0) \exp(-\tau/\tau_0)$ and the result was $\tau_0 = (5.64 \pm 0.02)$ ns. The lifetime of the excited state of the GeV center was reported to be 5 ns to 6 ns.[28,31] As expected, the spectral distribution and the excited state lifetime of the GeV center did not change significantly by the fabrication of the solid immersion lens around it.

In Fig. 7(d), the second-order correlation function is shown for continuous wave excitation. The measurement data were fitted using the Eq. (5) with the timing jitter measured above. The dip in the center goes down to $g^{(2)}(\tau = 0) = 0.12 \pm 0.06$. The simultaneous count rate at the detector, which is taken by removing the 50:50 beam splitter from the detection path and keeping the same excitation power, was measured to be 580 kcps. The second-order correlation was also measured with pulsed excitation at a repetition rate of $f_{\text{rep}} = 10$ MHz, which is shown in Fig. 7(e). Contrary to continuous wave excitation, for pulsed excitation, one can easily distinguish between uncorrelated background and correlated background events in the second-order correlation. Whereas the former would lift the whole curve by a constant offset, the latter is correlated to the peaks and, therefore, it increases the area of the innermost peak compared to the outer peaks. Therefore, the origin of the residual multi-photon events in this measurement must stem from some laser-correlated source, such as Raman scattered photons or secondary color centers

in the vicinity. From the Raman spectrum of diamond and the laser wavelength, we estimate second-order Raman scattered photons to have wavelengths up to 599 nm, which could still reach the detectors. The area under the centermost pulse divided by the average area under the outer pulses is a good estimator, resulting in $g^{(2)}(\tau = 0) = 0.16$. Nevertheless, the data were also fitted using a sum of Laplace distribution functions and a constant background factor, resulting in $g^{(2)}(\tau = 0) = 0.13 \pm 0.01$.

The saturation behavior of the GeV center was investigated by measuring the count rate at the detector for several excitation powers at the location of the SIL and in the background, roughly 1μm next to the emitter. Both measurements are shown in Fig. 7(f). The photon flux $N(P)$ depends on the laser power P and is assumed to be a sum of saturable emission from color centers and a linear signal from, e.g., Raman scattered photons. The equation

$$N(P) = \frac{N_{\text{sat}} P}{P + P_{\text{sat}}} + mP + dc \qquad (6)$$

describes this, where N_{sat} is the saturation count rate, P_{sat} the saturation laser intensity, m is the linear factor, and dc the dark count rate of the detector. Several values for $g^{(2)}(\tau = 0)$ were measured for different excitation powers and are shown in the same Fig. 7(f). It is possible to calculate the joint correlation function $g^{(2)}_{a,b}$ using the

equation[52]

$$g_{a,b}^{(2)} = \frac{g_a^{(2)} a^2 + 2ab + b^2}{(a+b)^2},$$ (7)

where a is the intensity of the emission from possibly multiple color centers, $g_a^{(2)}$ is their second order correlation function, and b is the intensity of some linear background signal. When a is assumed to be the first addend of Eq. (6) and b the second and third addend, the equation can be used to fit the values for $g^{(2)}(\tau = 0)$. This fit is shown in Fig. 7(f) as well. As a result, for the fit of the measurement at the emitter location using Eq. (6), the quotient $\frac{N_{sat}}{m}$ is fixed. The resulting values for the SIL were $N_{sat} = (854 \pm 8)$ kcps, $P_{sat} = (5.7 \pm 0.1)$ mW, $m = (3.0 \pm 2.1)(\mu W s)^{-1}$, and $g_a^{(2)} = 0.040 \pm 0.048$. This analysis suggests that the residual multi-photon emission probability might be due to a combination of other color centers ($g_a^{(2)} > 0$) and a linear signal ($m > 0$), e.g., Raman scattered photons. In Sec. IV D, further analysis of the multi-photon probability and its reduction by two methods is performed.

D. Residual $g^{(2)}(\tau = 0)$ analysis

Single photons from a GeV center can be distinguished from Raman scattered photons, stray light and emission from different color centers in multiple ways. There are two feasible ways in our setup: wavelength and time of arrival. First, with adequate spectral filtering, the GeV center emission could be separated from other photons, and second, in pulsed excitation, the timing of a detection event relative to the laser pulse can be used to filter events. The latter can lead to, e.g., an improvement of the $g^{(2)}(\tau = 0)$.[53,54] Both methods were used to analyze the properties of the background events that caused the residual $g^{(2)}(\tau = 0)$.

1. Spectral analysis

Suppose the residual $g^{(2)}(\tau = 0)$ is caused by photons that are distributed over a range of wavelengths, then the signal-to-noise ratio could increase by restricting the transmission band of the filtering system to the ZPL of the GeV center emission. The angles of the tunable edge-pass filters were set accordingly, which can be seen in the red curve in Fig. 7(b). Apart from that, the measurement conditions were the same. The second-order correlation function $g^{(2)}(\tau)$ of the ZPL emission is shown in Fig. 8. In comparison to the broader spectral distribution, the $g^{(2)}(\tau = 0)$ dropped to 0.07 ± 0.03, calculated from the fit, and 0.1 using the area method. The photon count rate decreased by roughly 60% due to spectral filtering of the ZPL. Even though this is a significant reduction of the $g^{(2)}(\tau = 0)$, large parts of the background photons must be in the ZPL wavelength range between 598 and 610 nm. The detector dark count rate cannot solely explain the residual value of $g^{(2)}(\tau = 0)$ in the ZPL emission. For comparison, Table I summarizes the results from this paper together with earlier results on germanium-vacancy centers in diamond from the literature.
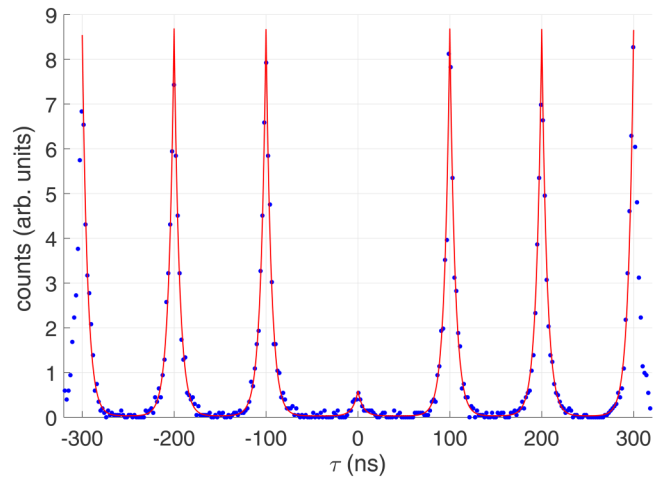

FIG. 8. The second-order correlation function $g^{(2)}(\tau)$ of the ZPL emission, measured with pulsed excitation at a repetition rate of $f_{rep} = 10$ MHz.

2. Temporal analysis

For the temporal analysis of the emission using a pulsed laser at a frequency of $f_{rep} = 10$ MHz, all detection event timestamps, as well as the timestamps of the laser trigger pulses, were collected with pico-second resolution and saved to the computer. The resulting data stream of approximately 80 million events were then analyzed in different ways. First, the stability of the source was estimated by calculating the count rate over time for such a measurement, which is shown in Fig. 9(a). The drift on larger timescales, e.g., between 0 and 450 s occurred due to the mechanical instability of the experimental setup. To compensate for the drift, the sample was moved, leading to a very short dip of the count rate and a leap back to a higher count rate. No blinking behavior of the color center itself was observed. The relative timing of the detection events was used to calculate the occupation probability of the excited state relative to the arrival of the laser pulse, resulting in the exponential decay curve shown in Fig. 9(b). The second-order correlation function was calculated from all events with a $g^{(2)}(\tau = 0) = 0.14$ using the area of the centermost peak divided by

TABLE I. Comparison of single-photon emission properties of the presented results with literature values. N_{sat} (kcps): count rate in saturation or the highest measured count rate, QE: quantum efficiency.

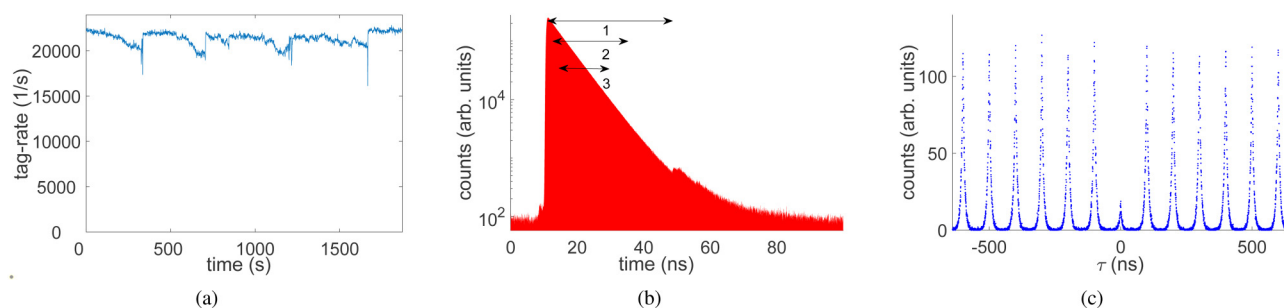| Publication	Type	N_{sat} (kcps)	QE (%)	$g^{(2)}(0)$
Iwasaki et al.[14]	Bulk	170		<0.5
Bhaskar et al.[55]	Waveguide	560 ± 20		0.08 ± 0.02
Siyushev et al.[15]	SIL	600		
Zhou et al.[16]	Bulk	178 ± 4		0.29 ± 0.04
Nguyen et al.[56]	Nanodiamond	714	22 ± 2	0.37 ± 0.02
Jensen et al.[29]	Open-cavity	0.38	17^{+8}_{-5}	0.25 ± 0.16
Nahra et al.[17]	Nanodiamond	1600		<0.5
This work	SIL	854 ± 8		0.13 ± 0.01

FIG. 9. Results of the temporal analysis of the GeV center emission: (a) the combined count rate on both detectors over time, (b) the decay curve of the excited state occupation, on which the acceptance windows were defined, and (c) the second-order correlation function $g^{(2)}(\tau)$ calculated from the event stream.

the average area of the outer peaks [see Fig. 9(c)]. This value matches the value calculated above, since the marginal difference can be explained by the varying experimental conditions.

The events were temporarily filtered using an acceptance window, which was defined by its center and width, and the filtered events were then used to calculate $g^{(2)}(\tau = 0)$. This calculation was done for a large number of window centers and widths, and the results are depicted in Fig. 10. Pixels with too few data points to be able to accurately calculate the second-order correlation function were blanked out. Three points in the 2D map are marked, which represent the highest single-photon purity in all window configurations that lead to an acceptance rate of at least 90%, 80%, and 50%, respectively. In Fig. 9(b), the intervals of these acceptance windows are shown in the decay curve. Table II gives an overview of their properties.

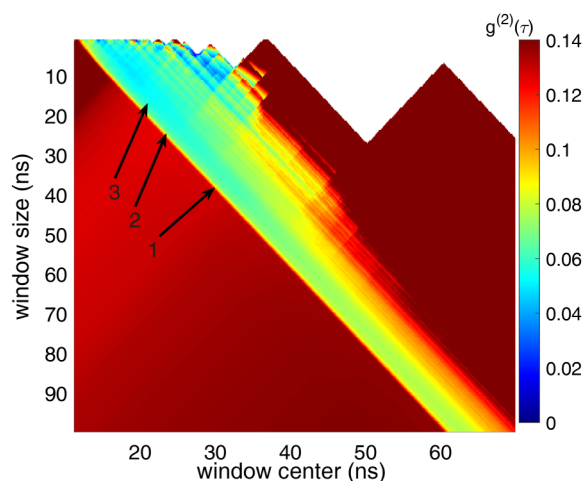The first window shows that by filtering only a small portion of all events, $g^{(2)}(\tau = 0)$ already drops significantly. With an acceptance rate of 80% the count rate in saturation from this emitter would be 666 kcps while the residual $g^{(2)}(\tau = 0)$ was cut in half. As expected, all windows completely filter out the dark count events before 10 ns and after roughly 70 ns. On a closer look, the rising side at 10 ns is also filtered. Here, we expect mostly photons to arrive, which are heavily correlated to the laser pulse, e.g., Raman photons. If only Raman photons would cause the residual multi-photon emission probability, we would expect $g^{(2)}(\tau = 0)$ to drop for longer times, when no Raman photons will arrive anymore. As this is not the case, but $g^{(2)}(\tau = 0)$ is in fact lowest for windows near the peak of the decay curve, we conclude that some non-zero emission from other fluorescing color centers, e.g., neighboring GeV centers, is present in the data. The overall shape of the 2D plot is not completely clear since we expect a complex combination of different effects, i.e., Raman photons, stray light, dark counts and neighboring GeV and other color centers.

E. System efficiency

The system efficiency, here defined as the probability that a laser pulse leads to a detection event that was produced by a GeV center emitted photon, is calculated in this section. To achieve this, the system efficiency SE_0 is factorized into the various sources of loss in the system

$$SE_0 = f_{ex} \times QE \times CE \times T \times SF \times DE, \qquad (8)$$

where f_{ex} is the probability that a laser pulse leads to the excitation of the GeV center, which is unity in saturation, and, therefore, the following calculations were carried out with saturation intensities. $QE = (22 \pm 2)\%$[56] is the quantum efficiency of the GeV center,

FIG. 10. 2D representation of the $g^{(2)}(\tau = 0)$ distribution for all acceptance windows. Three distinct acceptance windows marked with arrows (see text for explanation).

TABLE II. Properties of three acceptance windows and the resulting $g^{(2)}(\tau = 0)$ in comparison to the unfiltered value of $g^{(2)}(\tau = 0)$.

Acceptance window	none	1	2	3
Acceptance rate (%)		90	80	50
Window center (ns)		30.1	23.3	20.9
Window width (ns)		38.3	24.1	17.2
$g^{(2)}(\tau = 0)$	0.14	0.092	0.075	0.058

which includes non-radiative decay of the excited state. $CE = (27^{+0}_{-10})\%$ is the collection efficiency, which gives the proportion of photons that are emitted into the NA of the microscope objective and which was calculated in Sec. II B. The one-sided uncertainty was estimated to reflect the non-perfect fabrication of the SIL in the experiment. The factor T is the transmission coefficient of the whole setup with the fiber coupling included, and it was determined to be $T = (36 \pm 12)\%$. SF is the spectral filtering factor that gives the percentage of photons that are transmitted by the tunable edge filters. It is roughly $SF = (90 \pm 5)\%$. Finally, DE is the internal detection efficiency of the detectors, which is around $DE = (65^{+0}_{-10})\%$. The combined single-shot system efficiency is $SE_0 = (1.25^{+0.44}_{-0.67})\%$, where the uncertainty for some factors was estimated because it was not possible to calculate or measure them.

The saturation count rate of a two-level system can be expressed as[41]

$$N_{\text{sat}}(f_{\text{rep}}) = SE_0 \times f_{\text{rep}} \times \left(1 - \exp\left[-1/(\tau_{\text{eff}} \times f_{\text{rep}})\right]\right), \quad (9)$$

where τ_{eff} is the excited state lifetime. The saturation count rate was measured for several laser repetition rates, which is shown in Fig. 11. The system efficiency for higher repetition rates $SE(f_{\text{rep}})$ can also be measured directly by dividing N_{sat} by f_{rep}. Then, Eq. (9) gives

$$SE(f_{\text{rep}}) = SE_0 \times \left(1 - \exp\left[-1/(\tau_{\text{eff}} \times f_{\text{rep}})\right]\right). \quad (10)$$

For practical reasons, the system efficiency $SE = \frac{N_{\text{sat}}}{f_{\text{rep}}}$ could only be measured at repetition rates of some Megahertz and higher. To find the single-shot system efficiency SE_0, the measurements, shown in Fig. 11, were fitted using the Eqs. (9) and (10). The parameter τ_{eff} was not fixed to the excited state lifetime since the GeV center is not a two-level system, which is visible from the bunching behavior at intermediate times in the continuous wave
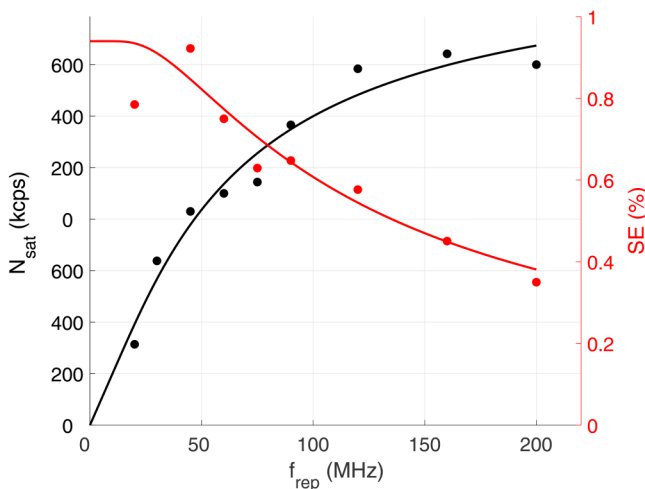
second-order correlation function in Fig. 7(d). Here, the metastable state of the GeV center simply leads to a higher effective lifetime. The system efficiency determined from the saturation count rate over the laser repetition rate was $SE_0 = (0.99 \pm 0.21)\%$, the effective lifetime was $\tau_{\text{eff}} = (10.7 \pm 3.6)$ ns and the saturation count rate for $f_{\text{rep}} \to \infty$ was (922 ± 194) kcps. The parameters determined from the system efficiency over the laser repetition rate were $SE_0 = (0.94 \pm 0.16)\%$, $\tau_{\text{eff}} = (9.6 \pm 2.9)$ ns, and $N_{\text{sat, inf}} = (977 \pm 170)$ kcps. The experimental single-shot system efficiencies and the value calculated from the sources of loss in the setup are in good agreement with each other, proofing the rigidity of the loss calculations.

The branching ratio of the excited state's decay into either the ground state (with the lifetime t_2) or the metastable state (with the lifetime t_3) was calculated from the effective lifetime t_0. We assume that the effective lifetime is the weighted mean of the two lifetimes t_2 and t_3, where the branching ratio is the weight parameter. Therefore, the branching ratio r_{21} is calculated from

$$r_{21} = \frac{\tau_{31} - \tau_{\text{eff}}}{\tau_{31} - \tau_{21}}, \quad (11)$$

where $\tau_{21} = (5.64 \pm 0.02)$ ns was determined in Sec. IV C. The lifetime of the metastable state can be calculated by examining the inverse lifetime in the continuous wave excitation second-order correlation measurement and extrapolating to zero excitation power.[24,35,57] This is shown in Fig. 12. The lifetime fit resulted in $\tau_{31} = 172.5$ ns.

The branching ratio r_{21} was calculated for τ_{eff} from the fit of the saturation count rate to be 96.9% and for the direct measurement of the system efficiency, it was $r_{21} = 97.6\%$. Even though this means that there was only a small probability for the excited state to decay into the metastable state, the total time the GeV was in the metastable state was relatively large due to its longer lifetime.
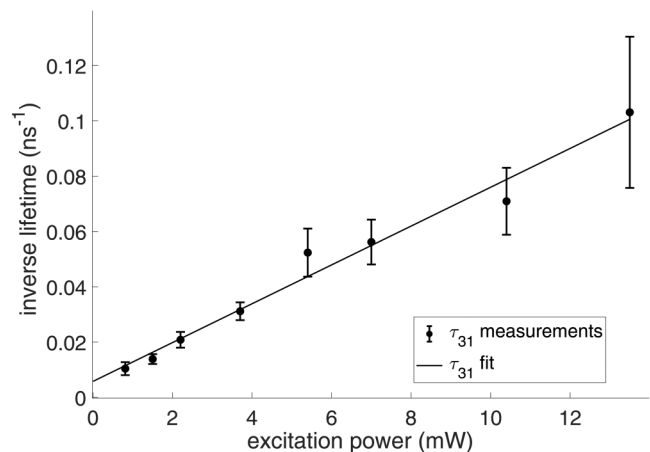
FIG. 11. The saturation count rate plotted over the laser repetition rate to determine the system efficiency.

FIG. 12. Inverse lifetime of the metastable state of the GeV center, calculated from the fit of the continuous wave excitation second-order correlation function measurement.
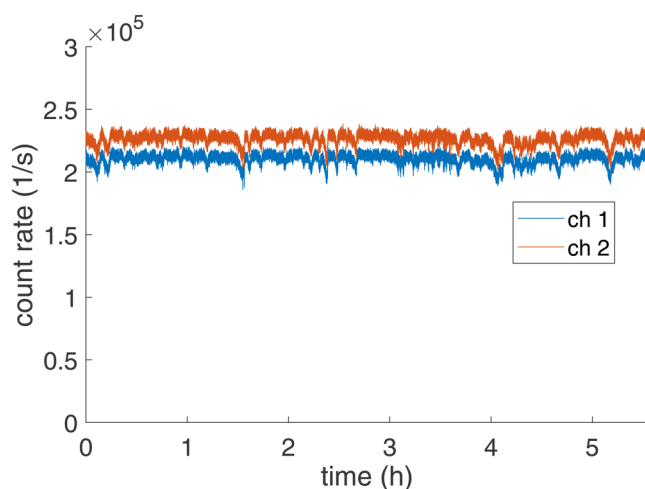
FIG. 13. Measurement of the temporal stability of the single-photon emission of the GeV center under a SIL on both channels of a Hanbury Brown and Twiss setup.

For the two methods, it was determined to be 49.1% and 42.8%, respectively. This calculation is valid for single-shot excitation of the GeV center, but it could, in principle, be made for higher laser repetition rates or even continuous wave excitation.

F. Temporal stability

The temporal stability of the single-photon source was investigated by measuring the count rate from the GeV center presented over a timespan of several hours, which can be seen in Fig. 13. The excitation laser power was set to roughly 7 mW, resulting in a total count rate of roughly 440 kcps on both channels summed up. It should be noted that due to mechanical instability of the setup, the color center was held in the focal volume of the confocal microscope by tiny re-alignments of the piezo scanner position, which caused some short dips of the count rate, e.g., at 1.5 and 5 h. Besides the realignments, the count rate was stable for these several hours, with no bleaching and no blinking in a time regime of more than 100 ms observed. Without mechanical stabilization, the count rate would deteriorate, typically within 10–60 min. These results match well with the already observed emission stability over shorter periods.[16] The fabrication of a solid immersion lens around the emitter seems not to have worsened the temporal stability, as expected.

V. SUMMARY AND CONCLUSION

We have presented the fabrication of germanium-vacancy centers in diamond by implantation of Ge ions at 3 MeV and subsequent high-temperature annealing. The successful sample fabrication was proven by the characterization of the photoluminescence of a germanium-vacancy center in the sample in a self-built confocal laser-scanning microscope setup. We have introduced the principle of a solid immersion lens and have shown the

microfabrication of such solid immersion lenses in a focused ion beam scanning electron microscope (FIB-SEM) setup. One germanium-vacancy center in a solid immersion lens was then optically characterized by the measurement of the spectral distribution, the exponential decay of the excited state, and the second-order correlation function under continuous wave excitation as well as in pulsed excitation and the saturation behavior. The saturation count rate was determined to be $N_{sat} = (854 \pm 8)$ kcps, which is a significant enhancement compared to germanium-vacancy centers without a solid immersion lens fabricated onto them. The enhancement factor can only be estimated to be around 3 to 5 since no direct comparison of the emission of a germanium-vacancy center before and after fabrication of the solid immersion lens was possible due to drifting of the ion beam in the FIB-SEM. This is in accordance with literature values between 3 and 8 for germanium-vacancy centers in diamond.[18] The Hanbury Brown and Twiss measurement revealed $g^{(2)}(\tau = 0) = 0.12 \pm 0.06$ with a simultaneous count rate of 580 kcps at the detector. The dynamic spectral filtering enabled the direct measurement of the zero-phonon line emission. An increase in the single-photon purity was found, although there was still a significant background signal measured in the form of non-zero residual $g^{(2)}(\tau = 0)$. A 2D temporal analysis of the detection events in an 80 million event stream was performed. The detection events were filtered using an acceptance window for the relative timing of the detection event and the excitation laser pulse. A large part of the non-zero multi-photon probability could be attributed to detection events that were tightly correlated with the laser pulse in the time domain, e.g., Raman scattered photons. Still, some photons must stem from other fluorescence sources, such as neighboring germanium-vacancy centers. Finally, the system efficiency of the single-photon source was determined through the analysis of the saturation count rate over the excitation laser repetition rate. The experimentally derived value of roughly 1% matched with the value calculated from all sources of loss in the setup. This verified, on the one hand, the functionality of the solid immersion lens because the system efficiency could not reach such values without a SIL. On the other hand, it quantified possible ways of improvement through the reduction of one or more loss sources. The branching ratio of the excited state decay of the germanium-vacancy center was investigated and found to be heavily in favor of the single-photon emission, with only a fraction of the decay events going into the metastable state of the germanium-vacancy center. The long-term stability of the emission was shown over several hours. The presented single-photon source could be used for quantum radiometric experiments in the future, such as the calibration of the detection efficiency of single-photon avalanche diode detectors. Future development of single-photon sources with higher brightness could exploit other color centers, either with higher quantum efficiency, e.g., tin-vacancy centers[30] or lower excited state lifetime, e.g., lead-vacancy centers[31] or magnesium-vacancy centers.[26] Improvements are possible in the fabrication of a nanostructure to enhance the collection efficiency from the color center and to use the Purcell effect to enhance the emission rate. Here, structures such as the circular bullseye grating have been proven to increase the emission rate up to millions of counts.[58] Efforts should be made to fabricate a combination of both, a suitable color center and a suitable nanostructure, to

optimize the single-photon count rate and purity for quantum metrological experiments.

AUTHOR DECLARATIONS

Conflict of Interest

The authors have no conflicts to disclose.

Author Contributions

J. Christinck: Formal analysis (equal); Investigation (equal); Software (equal); Visualization (equal); Writing – original draft (equal). **F. Hirt:** Investigation (supporting); Writing – review & editing (equal). **H. Hofer:** Investigation (supporting); Writing – review & editing (equal). **Z. Liu:** Formal analysis (supporting); Investigation (supporting); Visualization (supporting); Writing – review & editing (equal). **M. Etzkorn:** Formal analysis (supporting); Investigation (supporting); Visualization (supporting); Writing – review & editing (equal). **T. Dunatov:** Investigation (supporting); Resources (equal); Writing – review & editing (equal). **M. Jakšic** Investigation (supporting); Resources (equal); Writing – review & editing (equal). **J. Forneris:** Investigation (supporting); Resources (equal); Writing – review & editing (equal). **S. Kück** Conceptualization (supporting); Funding acquisition (equal); Supervision (equal); Writing – review & editing (equal).

DATA AVAILABILITY

The data that support the findings of this study are available from the corresponding author upon reasonable request.

REFERENCES

[1] G. S. Buller and R. J. Collins, "Single-photon generation and detection," Meas. Sci. Technol. **21**, 012002 (2010).

[2] M. D. Eisaman, J. Fan, A. Migdall, and S. V. Polyakov, "Invited review article: Single-photon sources and detectors," Rev. Sci. Instrum. **82**, 071101 (2011).

[3] J. Y. Cheung, C. J. Chunnilall, E. R. Woolliams, N. P. Fox, J. R. Mountford, J. Wang, and P. J. Thomas, "The quantum candela: A re-definition of the standard units for optical radiation," J. Mod. Opt. **54**, 373–396 (2007).

[4] B. Rodiek, M. Lopez, H. Hofer, G. Porrovecchio, M. Smid, X.-L. Chu, S. Gotzinger, V. Sandoghdar, S. Lindner, C. Becher, and S. Kuck, "Experimental realization of an absolute single-photon source based on a single nitrogen vacancy center in a nanodiamond," Optica **4**, 71 (2017).

[5] F. Jelezko and J. Wrachtrup, "Single defect centres in diamond: A review," Physica Status Solidi (a) **203**, 3207–3225 (2006).

[6] V. M. Acosta, A. Jarmola, E. Bauch, and D. Budker, "Optical properties of the nitrogen-vacancy singlet levels in diamond," Phys. Rev. B **82**, 201202 (2010).

[7] F. M. Hossain, M. W. Doherty, H. F. Wilson, and L. C. L. Hollenberg, "*Ab initio* electronic and optical properties of the $N - V^-$ center in diamond," Phys. Rev. Lett. **101**, 226403 (2008).

[8] M. W. Doherty, N. B. Manson, P. Delaney, F. Jelezko, J. Wrachtrup, and L. C. Hollenberg, "The nitrogen-vacancy colour centre in diamond," Phys. Rep. **528**, 1–45 (2013).

[9] L. Rondin, J.-P. Tetienne, T. Hingant, J.-F. Roch, P. Maletinsky, and V. Jacques, "Magnetometry with nitrogen-vacancy defects in diamond," Rep. Prog. Phys. **77**, 056503 (2014).

[10] R. Schirhagl, K. Chang, M. Loretz, and C. L. Degen, "Nitrogen-vacancy centers in diamond: Nanoscale sensors for physics and biology," Annu. Rev. Phys. Chem. **65**, 83–105 (2014).

[11] J. Christinck, B. Rodiek, M. López, H. Hofer, H. Georgieva, and S. Kück, "Characterization of the angular-dependent emission of nitrogen-vacancy centers in nanodiamond," Appl. Phys. B **126**, 161 (2020).

[12] C. Li, R. Soleyman, M. Kohandel, and P. Cappellaro, "SARS-CoV-2 quantum sensor based on nitrogen-vacancy centers in diamond," Nano Lett. **22**, 43–49 (2022).

[13] C. Kurtsiefer, S. Mayer, P. Zarda, and H. Weinfurter, "Stable solid-state source of single photons," Phys. Rev. Lett. **85**, 290–293 (2000).

[14] T. Iwasaki, F. Ishibashi, Y. Miyamoto, Y. Doi, S. Kobayashi, T. Miyazaki, K. Tahara, K. D. Jahnke, L. J. Rogers, B. Naydenov, F. Jelezko, S. Yamasaki, S. Nagamachi, T. Inubushi, N. Mizuochi, and M. Hatano, "Germanium-vacancy single color centers in diamond," Sci. Rep. **5**, 12882 (2015).

[15] P. Siyushev, M. H. Metsch, A. Ijaz, J. M. Binder, M. K. Bhaskar, D. D. Sukachev, A. Sipahigil, R. E. Evans, C. T. Nguyen, M. D. Lukin, P. R. Hemmer, Y. N. Palyanov, I. N. Kupriyanov, Y. M. Borzdov, L. J. Rogers, and F. Jelezko, "Optical and microwave control of germanium-vacancy center spins in diamond," Phys. Rev. B **96**, 081201 (2017).

[16] Y. Zhou, Z. Mu, G. Adamo, S. Bauerdick, A. Rudzinski, I. Aharonovich, and W.-B. Gao, "Direct writing of single germanium vacancy center arrays in diamond," New J. Phys. **20**, 125004 (2018).

[17] M. Nahra, D. Alshamaa, R. Deturche, V. Davydov, L. Kulikova, V. Agafonov, and C. Couteau, "Single germanium vacancy centers in nanodiamonds with bulk-like spectral stability," AVS Quantum Sci. **3**, 012001 (2021).

[18] D. Chen, J. Froech, S. Ru, H. Cai, N. Wang, G. Adamo, J. Scott, F. Li, N. Zheludev, I. Aharonovich, and W.-B. Gao, "Quantum interference of resonance fluorescence from germanium-vacancy color centers in diamond," arXiv:2202.07906 [cond-mat, physics:quant-ph] (2022).

[19] T. Iwasaki, Y. Miyamoto, T. Taniguchi, P. Siyushev, M. H. Metsch, F. Jelezko, and M. Hatano, "Tin-vacancy quantum emitters in diamond," Phys. Rev. Lett. **119**, 253601 (2017).

[20] M. E. Trusheim, B. Pingault, N. H. Wan, M. Gündoğan, L. De Santis, R. Debroux, D. Gangloff, C. Purser, K. C. Chen, M. Walsh, J. J. Rose, J. N. Becker, B. Lienhard, E. Bersin, I. Paradeisanos, G. Wang, D. Lyzwa, A. R.-P. Montblanch, G. Malladi, H. Bakhru, A. C. Ferrari, I. A. Walmsley, M. Atatüre, and D. Englund, "Transform-limited photons from a coherent tin-vacancy spin in diamond," Phys. Rev. Lett. **124**, 023602 (2020).

[21] P. Fuchs, T. Jung, M. Kieschnick, J. Meijer, and C. Becher, "A cavity-based optical antenna for color centers in diamond," APL Photonics **6**, 086102 (2021).

[22] J. Görlitz, D. Herrmann, G. Thiering, P. Fuchs, M. Gandil, T. Iwasaki, T. Taniguchi, M. Kieschnick, J. Meijer, M. Hatano, A. Gali, and C. Becher, "Spectroscopic investigations of negatively charged tin-vacancy centres in diamond," New J. Phys. **22**, 013048 (2020).

23. J. Görlitz, D. Herrmann, P. Fuchs, T. Iwasaki, T. Taniguchi, D. Rogalla, D. Hardeman, P.-O. Colard, M. Markham, M. Hatano, and C. Becher, "Coherence of a charge stabilised tin-vacancy spin in diamond," npj Quantum Inf. 8, 45 (2022).

24. S. Ditalia Tchernij, E. Corte, T. Lühmann, P. Traina, S. Pezzagna, I. P. Degiovanni, G. Provatas, E. Moreva, J. Meijer, P. Olivero, M. Genovese, and J. Forneris, "Spectral features of Pb-related color centers in diamond—A systematic photoluminescence characterization," New J. Phys. 23, 063032 (2021).

25. P. Wang, T. Taniguchi, Y. Miyamoto, M. Hatano, and T. Iwasaki, "Low-temperature spectroscopic investigation of lead-vacancy centers in diamond fabricated by high-pressure and high-temperature treatment," ACS Photonics 8, 2947–2954 (2021).

26. E. Corte, G. Andrini, E. Nieto Hernández, V. Pugliese, Â. Costa, G. Magchiels, J. Moens, S. M. Tunhuma, R. Villarreal, L. M. C. Pereira, A. Vantomme, J. G. Correia, E. Bernardi, P. Traina, I. P. Degiovanni, E. Moreva, M. Genovese, S. Ditalia Tchernij, P. Olivero, U. Wahl, and J. Forneris, "Magnesium-vacancy optical centers in diamond," ACS Photonics 10, 101–110 (2022).

27. B. Rodiek, M. López, H. Hofer, and S. Kück, "The absolutely characterized nitrogen vacancy center-based single-photon source—Measurement uncertainty of photon flux and angular emission properties," J. Phys.: Conf. Ser. 972, 012008 (2018).

28. C. Bradac, W. Gao, J. Forneris, M. E. Trusheim, and I. Aharonovich, "Quantum nanophotonics with group IV defects in diamond," Nat. Commun. 10, 5625 (2019).

29. R. H. Jensen, E. Janitz, Y. Fontana, Y. He, O. Gobron, I. P. Radko, M. Bhaskar, R. Evans, C. D. Rodríguez Rosenblueth, L. Childress, A. Huck, and U. Lund Andersen, "Cavity-enhanced photon emission from a single germanium-vacancy center in a diamond membrane," Phys. Rev. Appl. 13, 064016 (2020).

30. P. K. Shandilya, S. Flagan, N. C. Carvalho, E. Zohari, V. K. Kavatamane, J. E. Losby, and P. E. Barclay, "Diamond integrated quantum nanophotonics: Spins, photons and phonons," J. Lightwave Technol. 40(23), 1–33 (2022).

31. G. Thiering and A. Gali, "Ab initio magneto-optical spectrum of group-IV vacancy color centers in diamond," Phys. Rev. X 8, 021063 (2018).

32. A. M. Zaitsev, Optical Properties of Diamond (Springer, Berlin, 2001).

33. W. Barnes, G. Björk, J. Gérard, P. Jonsson, J. Wasey, P. Worthing, and V. Zwiller, "Solid-state single photon sources: Light collection strategies," Eur. Phys. J. D - At., Mol. Opt. Phys. 18, 197–210 (2002).

34. S. Castelletto, J. P. Harrison, L. Marseglia, A. C. Stanley-Clarke, B. C. Gibson, B. A. Fairchild, J. P. Hadden, Y.-L. D. Ho, M. P. Hiscocks, K. Ganesan, S. T. Huntington, F. Ladouceur, A. D. Greentree, S. Prawer, J. L. O'Brien, and J. G. Rarity, "Diamond-based structures to collect and guide light," New J. Phys. 13, 025020 (2011).

35. A. Beveratos, R. Brouri, T. Gacoin, J.-P. Poizat, and P. Grangier, "Nonclassical radiation from diamond nanocrystals," Phys. Rev. A 64, 061802 (2001).

36. E. M. Purcell, "Spontaneous emission probabilities at radio frequencies," Phys. Rev. 69, 681 (1946).

37. P. Siyushev, F. Kaiser, V. Jacques, I. Gerhardt, S. Bischof, H. Fedder, J. Dodson, M. Markham, D. Twitchen, F. Jelezko, and J. Wrachtrup, "Monolithic diamond optics for single photon detection," Appl. Phys. Lett. 97, 241902 (2010).

38. D. Riedel, D. Rohner, M. Ganzhorn, T. Kaldewey, P. Appel, E. Neu, R. J. Warburton, and P. Maletinsky, "Low-loss broadband antenna for efficient photon collection from a coherent spin in diamond," Phys. Rev. Appl. 2, 064011 (2014).

39. J. Yang, C. Nawrath, R. Keil, R. Joos, X. Zhang, B. Höfer, Y. Chen, M. Zopf, M. Jetter, S. Luca Portalupi, F. Ding, P. Michler, and O. G. Schmidt, "Quantum dot-based broadband optical antenna for efficient extraction of single photons in the telecom O-band," Opt. Express 28, 19457 (2020).

40. W. Nie, N. L. Sharma, C. Weigelt, R. Keil, J. Yang, F. Ding, C. Hopfmann, and O. G. Schmidt, "Experimental optimization of the fiber coupling efficiency of GaAs quantum dot-based photon sources," Appl. Phys. Lett. 119, 244003 (2021).

41. T. Schröder, F. Gädeke, M. J. Banholzer, and O. Benson, "Ultrabright and efficient single-photon generation based on nitrogen-vacancy centres in nanodiamonds on a solid immersion lens," New J. Phys. 13, 055017 (2011).

42. J. P. Hadden, J. P. Harrison, A. C. Stanley-Clarke, L. Marseglia, Y.-L. D. Ho, B. R. Patton, J. L. O'Brien, and J. G. Rarity, "Strongly enhanced photon collection from diamond defect centers under microfabricated integrated solid immersion lenses," Appl. Phys. Lett. 97, 241901 (2010).

43. L. Marseglia, J. P. Hadden, A. C. Stanley-Clarke, J. P. Harrison, B. Patton, Y.-L. D. Ho, B. Naydenov, F. Jelezko, J. Meijer, P. R. Dolan, J. M. Smith, J. G. Rarity, and J. L. O'Brien, "Nanofabricated solid immersion lenses registered to single emitters in diamond," Appl. Phys. Lett. 98, 133107 (2011).

44. M. Jamali, I. Gerhardt, M. Rezai, K. Frenner, H. Fedder, and J. Wrachtrup, "Microscopic diamond solid-immersion-lenses fabricated around single defect centers by focused ion beam milling," Rev. Sci. Instrum. 85, 123703 (2014).

45. J. F. Ziegler, M. Ziegler, and J. Biersack, "SRIM—The stopping and range of ions in matter (2010)," Nucl. Instrum. Methods Phys. Res. Sect. B: Beam Interact. Mater. At. 268, 1818–1823 (2010).

46. F. Hirt, J. Christinck, H. Hofer, B. Rodiek, and S. Kueck, "Sample fabrication and metrological characterization of single-photon emitters based on nitrogen vacancy centers in nanodiamonds," Eng. Res. Express 3, 045038 (2021).

47. E. Neu, R. Albrecht, M. Fischer, S. Gsell, M. Schreck, and C. Becher, "Electronic transitions of single silicon vacancy centers in the near-infrared spectral region," Phys. Rev. B 85, 245207 (2012). arxiv:1204.4994.

48. S. Castelletto, F. A. Inam, S.-I. Sato, and A. Boretti, "Hexagonal boron nitride: A review of the emerging material platform for single-photon sources and the spin–photon interface," Beilstein J. Nanotechnol. 11, 740–769 (2020).

49. J. Christinck, B. Rodiek, M. López, H. Georgieva, H. Hofer, S. Götzinger, and S. Kück, "Comparison of back focal plane imaging of nitrogen vacancy centers in nanodiamond and core-shell CdSe/CdS quantum dots," J. Phys.: Conf. Ser. 2149, 012014 (2022).

50. H. Georgieva, M. López, H. Hofer, J. Christinck, B. Rodiek, P. Schnauber, A. Kaganskiy, T. Heindel, S. Rodt, S. Reitzenstein, and S. Kück, "Radiometric characterization of a triggered narrow-bandwidth single-photon source and its use for the calibration of silicon single-photon avalanche detectors," Metrologia 57, 055001 (2020).

51. M. López, B. Rodiek, and S. Kück, "Coupling efficiency from the emitter to a detector, Published: EMRP JRP - EXL02 SIQUTE, D1.2.9," (2015).

52. A. W. Schell, J. Kaschke, J. Fischer, R. Henze, J. Wolters, M. Wegener, and O. Benson, "Three-dimensional quantum photonic elements based on single nitrogen vacancy-centres in laser-written microstructures," Sci. Rep. 3, 1577 (2013).

53. T. Kupko, M. von Helversen, L. Rickert, J.-H. Schulze, A. Strittmatter, M. Gschrey, S. Rodt, S. Reitzenstein, and T. Heindel, "Tools for the performance optimization of single-photon quantum key distribution," npj Quantum Inf. 6, 29 (2020).

54. T. Gao, M. von Helversen, C. Antón-Solanas, C. Schneider, and T. Heindel, "Atomically-thin single-photon sources for quantum communication," npj 2D Mater. Appl. 7, 4 (2023).

55. M. K. Bhaskar, D. D. Sukachev, A. Sipahigil, R. E. Evans, M. J. Burek, C. T. Nguyen, L. J. Rogers, P. Siyushev, M. H. Metsch, H. Park, F. Jelezko, M. Lončar, and M. D. Lukin, "Quantum nonlinear optics with a germanium-vacancy color center in a nanoscale diamond waveguide," Phys. Rev. Lett. 118, 223603 (2017).

56. M. Nguyen, N. Nikolay, C. Bradac, M. Kianinia, E. A. Ekimov, N. Mendelson, O. Benson, and I. Aharonovich, "Photodynamics and quantum efficiency of germanium vacancy color centers in diamond," Adv. Photonics 1, 1 (2019).

57. E. Corte, S. Sachero, S. Ditalia Tchernij, T. Lühmann, S. Pezzagna, P. Traina, I. P. Degiovanni, E. Moreva, P. Olivero, J. Meijer, M. Genovese, and J. Forneris, "Spectral emission dependence of tin-vacancy centers in diamond from thermal processing and chemical functionalization," Adv. Photonics Res. 3, 2100148 (2022).

58. L. Li, E. H. Chen, J. Zheng, S. L. Mouradian, F. Dolde, T. Schröder, S. Karaveli, M. L. Markham, D. J. Twitchen, and D. Englund, "Efficient photon collection from a nitrogen vacancy center in a circular bullseye grating," Nano Lett. 15, 1493–1497 (2015).